Manuscript

Simulation of overtopping and seepage induced dike failure using two-point MPM

Dongfang Liang[a,*], Xuanyu Zhao[a], Kenichi Soga[b]

[a]Department of Engineering, University of Cambridge, Trumpington Street, Cambridge, CB2 1PZ, UK

[b]Department of Civil and Environmental Engineering, University of California-Berkeley, Berkeley, CA 94720, USA

Email: dl359@cam.ac.uk

ABSTRACT

Fluvial dikes are important engineering works for protecting river valleys from flooding, so the stability of them is of great importance. In this paper, we apply a two-point two-phase formulation of the Material Point Method (MPM) to investigate the dike stability problem under the action of overtopping flows. Such a method has been incorporated in the Anura3D software (www.anura3d.com). In the model, the behaviours of soil and water are analysed in a single framework, so the interactions between the two phases are fully dynamic. The computational results agree well with the laboratory experiments. Parametric studies have been carried out to examine the effectiveness of various dike stability measures. The two-point MPM shows encouraging capabilities for studying a broad range of phenomena involving strong soil/water interactions.

Keywords: material point method; dike stability; overtopping; seepage; soil/water interaction

1. INTRODUCTION

Fluvial dikes are among the oldest inventions in river and reservoir engineering (Hager, 2016) and they are crucial infrastructures in flood risk management. Failures of dikes can cause tremendous damage to the local economy and society. During the well-recorded landslide-induced overtopping in the Vajont reservoir in Italy in 1963, the flood wave destroyed the city of Longarone, killing 2,000 people (Panizzo *et al.*, 2005). The majority of dikes and earthen embankments will breach in the occurrence of overtopping or a combination of overtopping and internal erosion (Singh, 1996). During Hurricane Katrina in New Orleans in 2005, fifty dike breaches took place, of which forty breaches were due to overtopping (Daniel, 2007).

Internal erosion occurs when the seepage flow through or beneath the dike is sufficiently strong to detach soil particles from the soil matrix inside the dyke. Internal erosion is especially dangerous because there may be no apparent sign of dyke failure. According to ICOLD (2013), there are four internal erosion mechanisms: (a) concentrated leak, where seeping water erodes and enlarges a crack until a breach occurs, (b) backward erosion, which is initiated at the exit point of the seepage path and develops progressively backwards, (c) contact erosion, which takes place at the interface between coarse and fine soils, and (d) suffusion, which occurs in non-cohesive soils with a wide range of particle sizes resulting in the fine particles to be smaller than the void space between coarse particles. Dike overtopping initiates when the elevation of the dike crest is exceeded by the floodwater level. Chinnarasri *et al.*, (2003) observed four stages in plane dike erosion: (a) small erosion on a dike crest after initial overtopping, (b) slope sliding failure with ongoing erosion, (c) wavelike-shaped dike profiles, and (d) large sediment wedge deposition with a small slope at the erosion end.

Researchers from the Laboratory of Hydraulics, Hydrology and Glaciology (VAW) at ETH Zurich conducted systematic studies of dike overtopping in different scenarios, e.g., constant approaching flow rates (Schmocker and Hager, 2009, 2012; Schmocker, 2011; Schmocker et al., 2014; Hager, 2016), constant headwater elevations (Hager, 2016) and solitary wave attacks (Huber et al., 2017). Schmocker and Hager (2009) focused on scale effects in laboratory dike-breach tests and revealed model limitations for dike-breach experiments. To be able to ignore the scale effect, the results provided suggestions on the minimum values of the dike height and width, sediment diameter and overtopping discharge. Schmocker and Hager (2012) found that the sediment diameter has a decisive effect on the breach process. After the initial overtopping phase, the dike erosion process is decelerated with increasing sediment size, as the erosion is now mainly controlled by sediment transport. A systematic variation of the dike dimensions, the sediment diameter and the inflow discharge resulted in basic findings concerning the breach discharge and the dike failure. The governing parameters of the dike-breach process were found to include the dike height, the grain size and the critical flow depth.

Huber et al. (2017) investigated the effect of a solitary wave overtopping a granular dam. Wave overtopping leads to large damage or even dam breach. The data analysis gave rise to empirical formulae for (a) the overtopping depth, (b) the overtopping volume, (c) the wave overtopping duration, (d) the eroded crest depth, (e) the eroded dam area, and (f) the deposited dam area. The results allowed for the prediction of the above parameters based on the governing parameters. Overtopping breaching of cohesive embankments is a more complex phenomenon (Wei *et al.*, 2016). Many studies of the cohesive embankments/dikes have also been conducted with the results of non-cohesive embankments serving as references. Readers are referred to Zhu (2006) and Wei et al. (2016) for further information.

In contrast to the extensive experimental studies, there have been little numerical investigations of the overtopping induce dam failure phenomena. Recently, the meshfree methods have been increasingly applied to the large deformation and strong soil/water interaction processes. The material point method (MPM) has been used to solve multiphase problems in saturated and unsaturated porous media, e.g., Abe, Soga and Bandara (2013), Yerro, Alonso and Pinyol (2015), Zhao and Liang (2016). The interaction between the two phases has been formulated in two different manners. One manner is to adopt only one set of Material Points (MPs) in the so-called one-point formulation, e.g., Alonso and Zabala (2011), Jassim, Stolle and Vermeer (2013). The other manner is to adopt two sets of MPs in the so-called two-point formulation, e.g., Więckowski (2013) , Martinelli (2016). The two sets of MPs are used to calculate the velocities of the solid skeleton and water separately, and they are allowed to move independently and to overlap. Hence, the two-point formulation gives a better representation of the relative movement between soil and water. When the two sets of particles occupy the same region, then the soil becomes saturated. The method is capable of simulating the conversion between dry soil and saturated soil and between interstitial water and free water (the water not being confined in the soil skeleton).

In this study, the fundamental principles of the two-point MPM were first reviewed, followed by the introduction of the inflow/outflow boundary conditions for generating unidirectional incoming flows. Next, the two-point MPM simulation was set up for the dike overtopping problems and verified against laboratory measurements. This computational model was then applied to analyse the effects of the bottom drainage, protection methods and critical drainage capacities to dike stability. The merits of the current formulation were highlighted through these example studies.

2. TWO-POINT MPM

Overview

The one-point two-phase formulation relies on the Eulerian formulation to describe the relative movement between water and soil, which becomes difficult when the relative movement between the two phases is large or when there is a sharp interface between two phases. In order to address this challenge and fully take advantage the Lagrangian formulation, the two-point MPM formulation was proposed (Abe et al., 2013; Vermeer *et al.*, 2013; Bandara and Soga, 2015). In the two-point MPM framework, the solid skeleton and the water phase are separately represented by two sets of MPs which are allowed to occupy the same location at the same time to denote the existence of pore water in the soil skeleton. When the soil and water particles do not coincide, then they represent either dry soil or pure water. We do not consider the complicated unsaturated soil behaviour in this paper.

There are two sets of primary unknowns to be determined. Hence, the mechanical response of the dry soil, saturated soil, free-surface water and ground water can all be modelled in a unified framework. In the double-point MPM formulation, the governing equations can be categorised into the mass balance equations, the momentum balance equations and the constitutive equations of the materials. In the following, the quantities associated with the solid phase and liquid phase are referred to by subscripts *S* and *L*, respectively.

Mass conservation equations

The mass balance equations are also referred to as the continuity equations or the mass conservation equations, which can be written as:

$$\frac{d(n\rho_{\mathrm{L}})}{dt} + n\rho_{\mathrm{L}}\nabla\cdot\mathbf{V}_{\mathrm{L}} = 0 \tag{1}$$

$$\frac{d[(1-n)\rho_{\mathrm{S}}]}{dt} + (1-n)\rho_{\mathrm{S}}\nabla\cdot\mathbf{V}_{\mathrm{S}} = 0 \tag{2}$$

where n is the porosity, ρ is the density, $\mathbf{V}$ is the velocity vector. The porosity n can also be regarded as the liquid concentration ratio defined as the ratio between the macroscopic partial density of liquid $\bar{\rho}_{\mathrm{L}}$ and the true liquid density ρ_{L}. Similarly, $(1-n)$ can be understood as the solid concentration ratio of the solid phase which is defined as the ratio between the macroscopic solid partial density $\bar{\rho}_{\mathrm{S}}$ and the true solid density ρ_{S} (Martinelli, 2016).

Assuming negligible spatial variability of the liquid density, i.e. $\nabla\rho_{\mathrm{L}}$ is approximately zero, and incompressible solid grains, i.e. ρ_{S} remains constant, the equation for the volumetric strain rate of the weakly compressible liquid can be derived from the mass conservation equations as follows:

$$\frac{d\varepsilon_{\mathrm{vol,L}}}{dt} = \frac{1}{n}[(1-n)\nabla\cdot\mathbf{V}_{\mathrm{S}} + n\nabla\cdot\mathbf{V}_{\mathrm{L}} + \nabla n\cdot(\mathbf{V}_{\mathrm{L}} - \mathbf{V}_{\mathrm{S}})] \tag{3}$$

Momentum conservation equations

In this formulation, the momentum conservation equations are solved to obtain the acceleration of the solid skeleton and the fluid phase separately. The momentum exchange (or the interaction force) between the two phases is considered in terms of the drag force. Where water and soil particles coexist in an element, Terzaghi's effective stress concept is adopted for the mechanical response of the soil skeleton unless the soil grains are fluidised, in which case the intergranular force becomes zero and the soil particles move under the action of the submerged weight and the flow-induced drag force only.

$$n\rho_{\mathrm{L}}\frac{D\mathbf{V}_{\mathrm{L}}}{Dt} = \nabla\cdot(n\boldsymbol{\sigma}_{\mathrm{L}}) + n\rho_{\mathrm{L}}\mathbf{g} - (\mathbf{f}_{\mathrm{d}} + \boldsymbol{\sigma}_{\mathrm{L}}\cdot\nabla n) \tag{4}$$

$$(1-n)\rho_{\mathrm{S}}\frac{D\mathbf{V}_{\mathrm{S}}}{Dt} = \nabla\cdot[\boldsymbol{\sigma}_{\mathrm{S}}{}' + (1-n)\boldsymbol{\sigma}_{\mathrm{L}}] + (1-n)\rho_{\mathrm{S}}\mathbf{g} + (\mathbf{f}_{\mathrm{d}} + \boldsymbol{\sigma}_{\mathrm{L}}\cdot\nabla n) \tag{5}$$

where $\boldsymbol{\sigma}_{\mathrm{L}}$ is the stress tensor of the liquid phase (including the pore pressure p_{L} and the deviatoric stress), $\boldsymbol{\sigma}_{\mathrm{S}}{}'$ is the effective stress tensor and $\mathbf{g}$ is the gravity vector. The drag force $\mathbf{f}_{\mathrm{d}}$ is the force between the solid skeleton and the moving liquid. It depends on the permeability of the solid skeleton, the liquid viscosity and the relative velocity between liquid and solid phases. Ergun's law is used as follows (Martinelli, 2016).

$$\mathbf{f}_{\mathrm{d}} = n^2[\frac{\mu}{\kappa} + n\rho_{\mathrm{L}}\frac{F}{\sqrt{\kappa}}|\mathbf{V}_{\mathrm{L}} - \mathbf{V}_{\mathrm{S}}|](\mathbf{V}_{\mathrm{L}} - \mathbf{V}_{\mathrm{S}}) \tag{6}$$

where κ is the soil intrinsic permeability. The Kozeny-Carman formula is used to update the soil intrinsic permeability:

$$\kappa = \frac{{D_p}^2}{A}\frac{n^2}{(1-n)^2} \tag{7}$$

where D_{p} is the grain diameter and the constant A is set to 150 according to Ergun (1952). The coefficient F in Equation (3) is computed as:

$$F = \frac{B}{\sqrt{A}n^{1.5}} \tag{8}$$

where B is a constant set to 1.75 (Ergun, 1952). For the detailed description of the algorithms, readers are referred to Martinelli and Rohe (2015) and Fern *et al.* (2019).

Constitutive equations

The stress within the soil material is dependent on the soil constitutive model. The liquid material is assumed to be weakly compressible, whose mean stress (pressure) is determined by the liquid bulk modulus and volumetric strain (or density changes). The deviatoric stress tensor of the fluid is determined by the fluid viscosity coefficient and shear strain rate tensor. The constitutive equations for liquid phase and solid phase can be expressed as:

$$\Delta p_{\mathrm{L}} = K_{\mathrm{L}}\Delta\varepsilon_{\mathrm{vol,L}} \tag{9}$$

$$\Delta\boldsymbol{\sigma}_{\mathrm{S}} = \mathbf{D}\cdot\Delta\boldsymbol{\varepsilon}_{\mathrm{S}} \tag{10}$$

where Δp_{L} is the pressure increment, K_{L} is the bulk modulus of the liquid, $\Delta\varepsilon_{\mathrm{vol,L}}$ is the incremental volumetric strain of the liquid, $\mathbf{D}$ is the tangent matrix defined by the constitutive model, $\Delta\boldsymbol{\sigma}_{\mathrm{S}}$ and $\Delta\boldsymbol{\varepsilon}_{\mathrm{S}}$ are the solid stress and strain increments, respectively. This study adopts the standard Mohr-Coulomb model to describe the mechanical behaviour of the solid phase. In cases of liquid and fluidised mixture, the deviatoric part of the stress tensor is calculated as:

$$\boldsymbol{\sigma}_{\mathrm{dev,L}} = 2\mu\boldsymbol{\varepsilon}_{\mathrm{dev,L}} \tag{11}$$

where μ is the dynamic viscosity coefficient, $\boldsymbol{\varepsilon}_{\mathrm{dev,L}}$ is the deviatoric component of the liquid strain rate.

Inflow/outflow boundary condition

The inflow/outflow boundary conditions are described in Zhao *et al.* (2019), which allows the dynamic addition and deletion water particles during the calculation. As shown in Fig. 1(a), an inlet layer of elements is patched to the original computational domain. When certain conditions are met, they will feed new particles to the system at specified velocities. At the outflow boundary, a layer of outlet elements is patched to the system, as shown in Fig. 1(b). The state of the elements is checked in each time step. If these elements are active, i.e. they contain MPs, then the MPs inside the outlet elements are removed. Readers are referred to Zhao *et al.* (2019)

for more information. Most of the previous MPM studies set up large water tanks to generate unidirectional flows. However, as water flows out of the tank, the water level gradually drops. The inflow/outflow boundary conditions reduce the computational costs by reducing the number of MPs, and more important enables the generation of true steady flows.

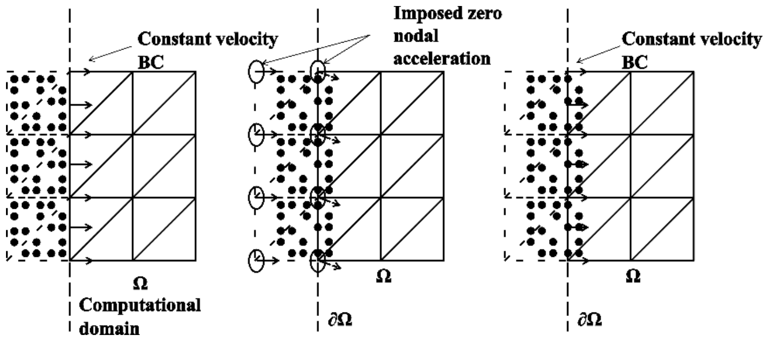

(a) Inflow condition

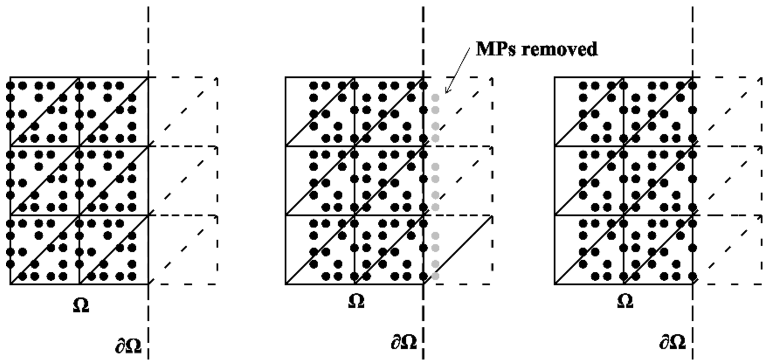

(b) Outflow condition

Fig. 1. Sketch of inflow and outflow boundary conditions

3. OVERTOPPING MODEL SETUP AND VERIFICATION

Experimental setup

The experimental setup of Test 52 in Schmocker (2011) is shown in Fig. 2. The sediment used was non-cohesive and no surface protection was added to the model dike. In the experiment, the BD (bottom drainage) was arranged beneath the upstream part of the dike, as illustrated in Fig. 2(a) by the dashed line. Steady discharge was added without any tailwater submergence and the filling procedure was relatively fast, typically within half a minute to fill the reservoir. Such fast filling and ensuing overtopping processes make it mandatory to adopt a fully-coupled soil/water model in the analyses and also help reduce the computational time.

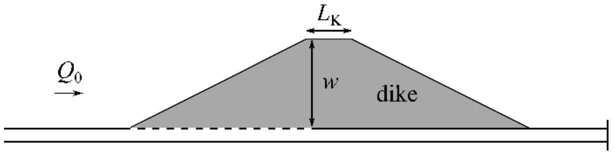

(a) Side view

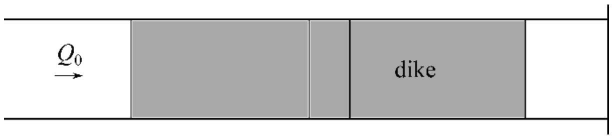

(b) Plan view

Fig. 2. Plane dike breach experiment conducted by Schmocker (2011)

In the experiment, a constant approaching discharge rate has been maintained with $Q_0 = 8$ l/s. The width of the flume and dike is 0.2 m, so the unit-width discharge is 0.04 m^2/s. Such a high flow rate resulted in dike overtopping at an instant assigned to be $t = 0$ s. At $t = 2$ s, erosion was observed at the downstream dike crest as the sediment transport was initiated. At this time, the overflow discharge was small and minor sediment accumulation as sediment was transported downward the dike face. The waterfront consisted of a sediment-water mixture, forming a debris flow. At $t = 4$ s the flow front reached the downstream dike toe and impacted on the channel bottom, leading to minor turbulence increase and air entrainment in this region ($t = 4$ s). Sediment was then eroded and transported along the downstream channel bed. The dike crest had already developed into a round shape. At $t = 6$ s, erosion advanced and the entire visible channel bottom was covered with the eroded material. A wavy deposition pattern was observed beyond the original dike toe. At $t = 20$ s, almost half of the dike was eroded. Up to this time, the thickness of the eroded material downstream of the original dike had kept increasing. From this point onwards, the erosion slowed down until the dike surface was nearly horizontal at $t = 100$ s. The eroded material formed a large tailwater wedge and the breach profile remained almost constant. A slightly three-dimensional erosion pattern was visible at $t = 200$ s and $t = 400$ s.

Computational setup

The computational mesh was constructed according to the experimental configuration, with the initial material assignment as illustrated in Fig. 3. The dike height $w = 0.2$ m and crest length $L_k = 0.1$ m. The dike was initially dry and filled with 10 solid Points Per Element (PPE). New liquid particles were generated from the inlet elements on the left boundary and flowed into the water tank at a constant rate Q_0. The outflow boundary condition was specified at the right end, where the free-surface flow leaves the computational domain. The right-end outflow boundary extended over the whole height of the domain.

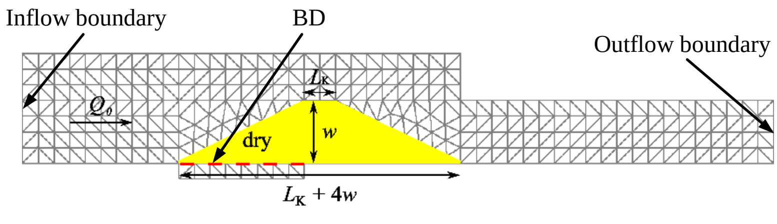

Fig. 3. Computational mesh

The BD was placed below the upstream half of the dike, as indicated by the red long-dashed line, to be consistent with the experiment. The BD was numerically treated in a similar way to aforementioned outflow boundary condition. Liquid MPs could freely penetrate the BD into the elements below it. Once the liquid MPs crossed the red long-dashed line downwards, then they would be removed from the domain and ceased to be involved in the computation anymore, while solid MPs were prohibited from passing through due to a vertical solid fixity at the location of the BD. The detailed material parameters of all the tests are listed in Table 1.

Table 1 Material parameters for the dike overtopping model validation

Material parameter	***Symbol***	***Values***	***Unit***
Soil:			
Density of soil grains	ρ_S	2,650	kg/m^3
Young's modulus	E	10,000	kPa
Poisson ratio of soil	v	0.3	-
Initial porosity	n	0.43	-
Friction angle	ϕ	30	^{o}
Threshold porosity	n_{max}	0.7	-
Solid grain diameter	D_p	2.0	mm
Water:			
Water density	ρ_L	1,000	kg/m^3
Water bulk modulus	K_L	20,000	kPa
Water dynamic viscosity	μ_L	1.0×10^{-6}	kPa·s

An important consideration in the two-point MPM is the state of the solid-liquid mixture, which is updated by monitoring the local porosity of the soil material. If the local porosity is low, then the grains are in contact and the behaviour of the mixture shall be determined by various constitutive models of the soil. Conversely, if the local porosity is very high, the collection of soil grains are not in contact with one another and thus no contact force exists any more. Then, the effective stresses are set to zero and the mixture is fluidised. The threshold porosity was often taken to be around 0.5 in previous studies (*e.g.* Martinelli and Rohe 2015, Martinelli 2016). However, those studies concern relatively small soil deformations, such as underwater landslides and slope instabilities. In the present study, the overtopping flow is accompanied by rapid sediment transport, so the accurate prediction of the flow traction force on the rapidly moving soil particles is extremely important. However, our current model does not consider the flow-induced shear stress on the solid particles. To mitigate this shortcoming, we adjusted the values of the threshold in a series of numerical experiments to find the optimum value that observe the correct sediment transport characteristics. The best match with experimental data was achieved when the threshold porosity for judging the state of the soil-water mixture was taken to be 0.7. Such a value was kept for all the following simulations, and the computational results were always found to be physically reasonable.

Fig. 4 shows the advance of the water table inside the dike as the upstream empty reservoir is filled. The overtopping starts at about 8.1 s after the filling, and that moment can be regarded as t = 0 s according to the aforementioned convention. In Fig. 4, the colour inside the dike corresponds to volume concentration of the liquid. Blue indicates zero liquid content (dry soil), while red indicates a liquid concentration of 0.43, which is equal to the initial porosity of the soil.

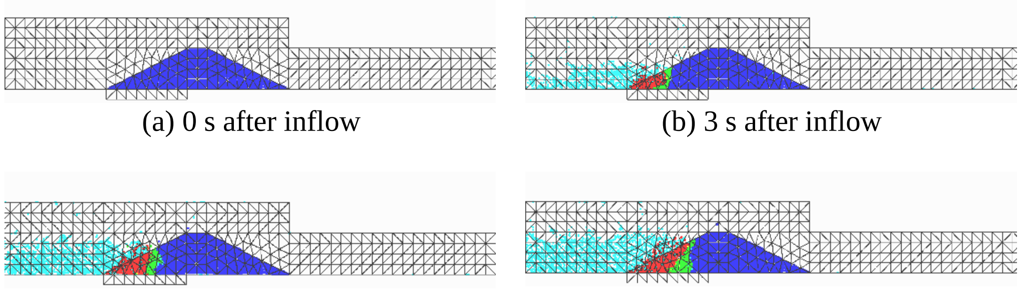

(a) 0 s after inflow

(b) 3 s after inflow

(c) 4 s after inflow (d) 5 s after inflow

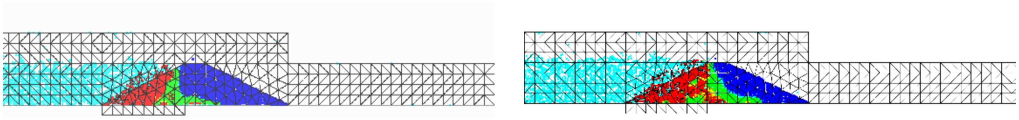

(e) 6.5 s after inflow (f) 8.1 s after inflow

Fig. 4. Evolution of water surface in the reservoir and inside dike (liquid concentration 

)

Comparison with experiments

The computed dike shape can be illustrated by an assemble of the discrete grey dots, as shown in Fig. 5. The measured dike profiles are superposed in Fig. 5 as black dotted lines. The rear face of the dike is seen to be gradually eroded and eventually failed, with a mixture of water and soil flowing downstream. At the same time, the water level in the reservoir keeps decreasing as time progresses, but the water particles are not plotted in Fig. 5 in order to keep the figure clear and simple. The predictions by the two-point MPM agree well with the experimental results reported in Schmocker (2011).

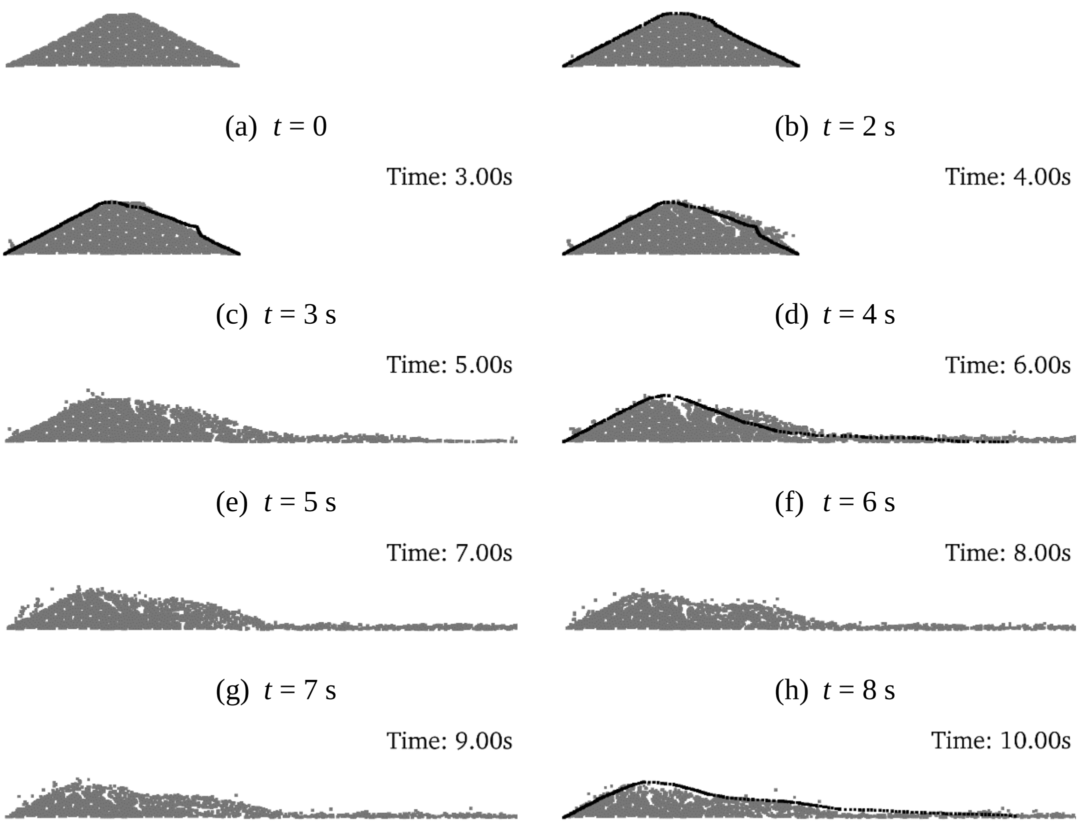

(a) $t = 0$ (b) $t = 2$ s (c) $t = 3$ s (d) $t = 4$ s (e) $t = 5$ s (f) $t = 6$ s (g) $t = 7$ s (h) $t = 8$ s (i) $t = 9$ s (j) $t = 10$ s

Fig. 5. Comparison between MPM results and experimental data

4. PARAMETRIC STUDY OF DIKE STABILITY

In this section, parametric studies are conducted, focusing on various topics related to the overtopping-induced and seepage-induced dike failures: 1) the BD location, 2) the drainage capacity, 3) the surface protection or core protection.

Modified initial condition

In order to reduce the computational cost in the parametric study, the reservoir was assumed to be initially full and correspondingly the upstream part of the dike was assumed to be initially fully-saturated, as shown in Fig. 6. The element colours represent different initial states and different allocations of the material points per element (PPE). Elements with green, blue and yellow were initially occupied by pure liquid (filled with 10 liquid PPE), saturated soil (10 liquid PPE & 10 solid PPE) and dry soil (10 solid PPE), respectively.

The validity of this assumption relies on the soil permeability and the length of the upstream reservoir. For this case study with the soil grain diameter of 2 mm, the assumption is rational as can be verified in Fig. 4. When overtopping was initiated at about 8.1 s after the filling, the computed liquid concentration in the dike (Fig. 4f) confirmed the correctness of the initial condition assignment illustrated in Fig. 6, i.e. overall the upstream half of the dike was fully saturated while the downstream half of the dike was nearly dry.

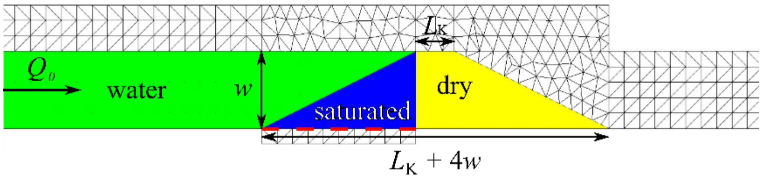

Fig. 6. Computational mesh and initial condition in the parametric study

Effects of bottom drainage location

In the experiments in Schmocker (2011), the BD was strangely placed underneath the upstream side of the dike, as illustrated in Fig. 3 by the red long-dashed line. In reality, the drainage commonly placed underneath the downstream side of the dike, e.g. below the yellow part of the dike in Fig. 6, to reduce the pore pressure in the downstream part of the dike to increase the dike stability against sliding. In this way, the drained water can be easily removed from inside the dike. Moreover, such an arrangement helps prevent any seepage exiting the downstream portion of the dam and avoid internal erosion (often called "piping") to make its way to the downstream surface. The effectiveness of the drainage in reducing pore pressures in the soil structure depends on the drain’s location and drainage length.

Mesh dependency studies have been conducted by Zhao (2019), which shows that the fine mesh resolution, as shown in Figs. 7(a-b), leads to similar predictions to the coarse mesh resolution, as shown in Figs. 7(c-e). Such results are achieved when each element can be occupied by 10 solid particles and 10 liquid particles.

Fig. 7 compares the deformation of the dike in three different drainage conditions, with the colours indicating the horizontal displacement. As expected, the dike failure developed earlier and faster when there is no BD at all. The BD delayed the dike failure process, no matter whether the BD is located upstream or downstream. As the seepage flow advanced downstream, the upstream BD would be more effective in the early stage than the downstream BD. With the existence of the upstream BD, the dike remained almost intact 3 s into the overtopping, as seen in Fig. 7(c). Some erosion was clearly noticeable at the downstream crest of the dike when the

BD was placed to be underneath the downstream part of the dike, as seen in Fig. 7 (e). Although the upstream BD successfully slowed down the progression of seepage flow and thus postponed the initial failure of the dike, it was less effective in the later stage, e.g. at t = 8 s. Comparing Figs. 7(d) and 7(f) clearly showed that the downstream BD performed better in keeping the overall integrity of the dike, which was consistent with the engineering practice in real world.

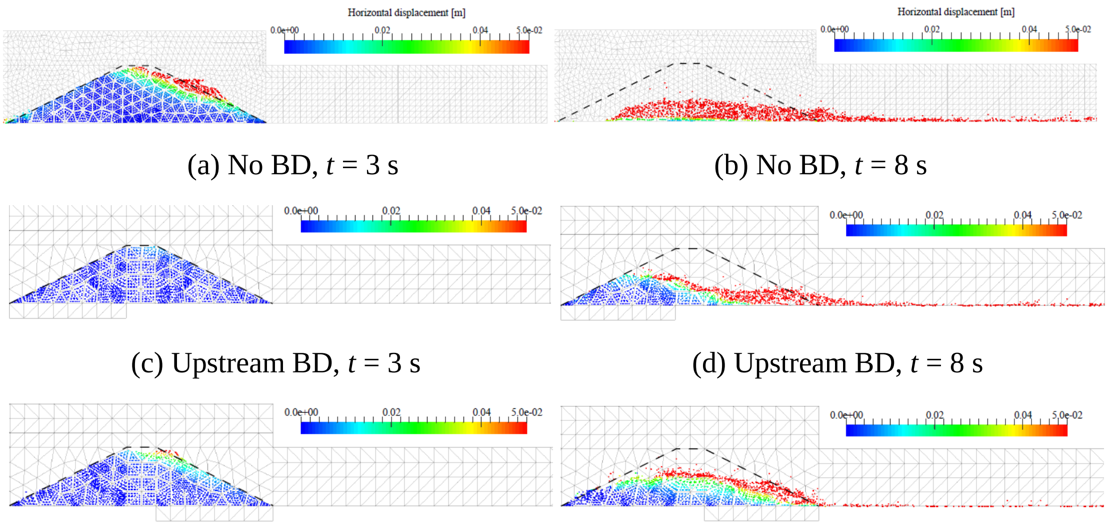

(a) No BD, t = 3 s (b) No BD, t = 8 s

(c) Upstream BD, t = 3 s (d) Upstream BD, t = 8 s

(e) Downstream BD, t = 3 s (f) Downstream BD, t = 8 s

Fig. 7. Comparison of the dike deformations with different drainage configurations (solid displacement in metres 0.0 0.02 0.04 0.05)

Effect of bottom drainage capacity

Drainage in the earthen embankment is used to bring the phreatic line within the downstream face of the structure, so that water does not seep through the embankment body. Excess water is drained from the bottom of the confining structures and thus reduces the pore pressure and thus the internal erosion. In engineering practices, drainage performance is often measured by the capacity of the system.

Simulations were carried out to study the effects of the maximum flow rate q_{max} of the BD on the stability of the dike. In these simulations, the BD was always located beneath the downstream part of the dike. Regardless the length of the BD, its downstream end always coincided with the downstream tip of the dike. By changing the length of the BD, various maximum drainage discharges were achieved, which was similar to adjusting the pumping capacity of the drainage system in the practice. In all the subsequent simulations, the initial condition is similar to that illustrated in Fig. 6, except that there is no incoming flow anymore. We examine the response of the dike under the action of a reservoir in its full capacity.

Figs. 8 and 9 show the distributions of liquid concentration and solid displacement, respectively, for cases with various BD lengths. In Fig. 8, the blue colour represents zero water content, while the red colour represents a value of 0.43, i.e. 43% of the volume in the dike is occupied by water. In Fig. 9, the blue colour represents zero soil displacement while the red colour indicates a displacement of 0.05 m. The evolution of the liquid content reveals the progression of the seepage flow, while the evolution of the solid displacement clearly reveals whether the dike is stable or not. When there is no BD, the seepage line arrives at the downstream dike toe at around 6 s. Then, the dike gradually fails. When the BD length is 10 cm, the seepage line cannot reach the downstream dike face at 6 s. However, the drainage capacity is not large enough to stop the seepage line intersecting the dike surface. As 10 s, the seepage line finally reaches the downstream dike face and leads to failure similar to the situation without BD. The existence of the insufficient BD can only delay the failure process. In the case of a BD length of 30 cm, the seepage line never reaches the downstream dike face because all the seepage water is drained by the BD. Hence, the dike stays stable during the whole process.

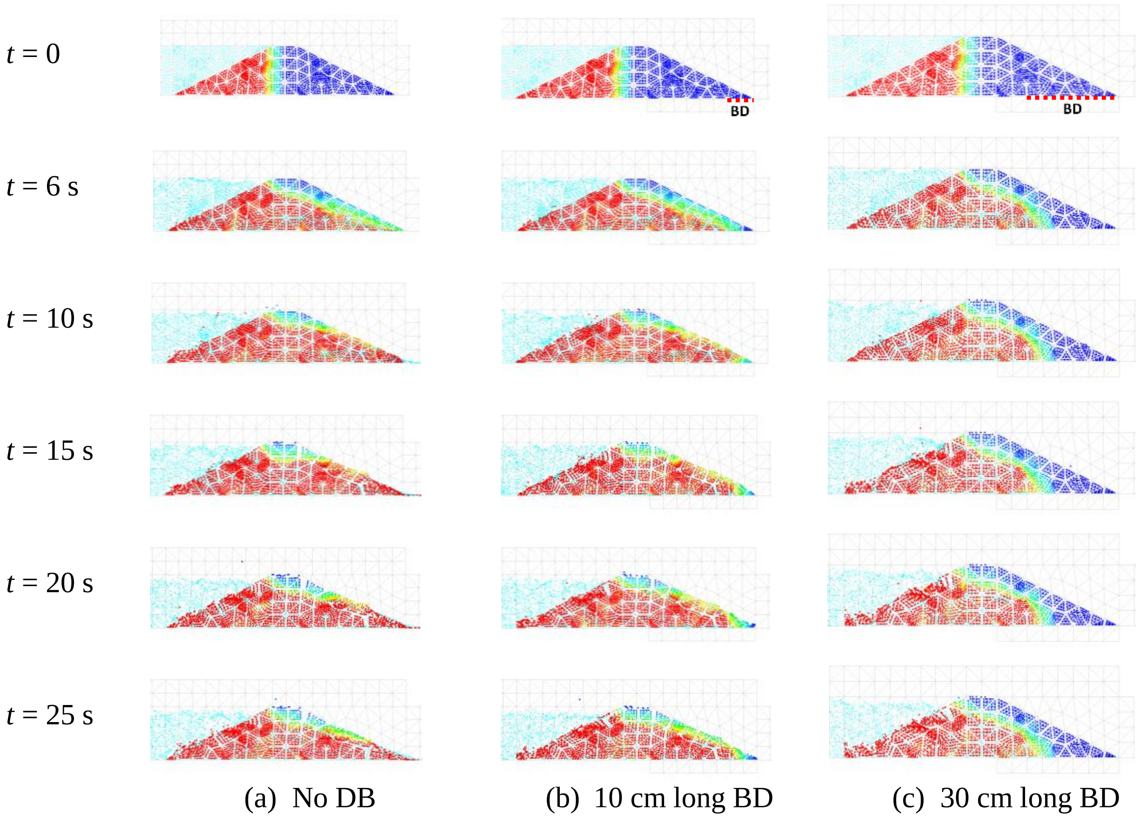

Fig. 8. Liquid concentration with different BD lengths (0.0 0.15 0.3 0.43)

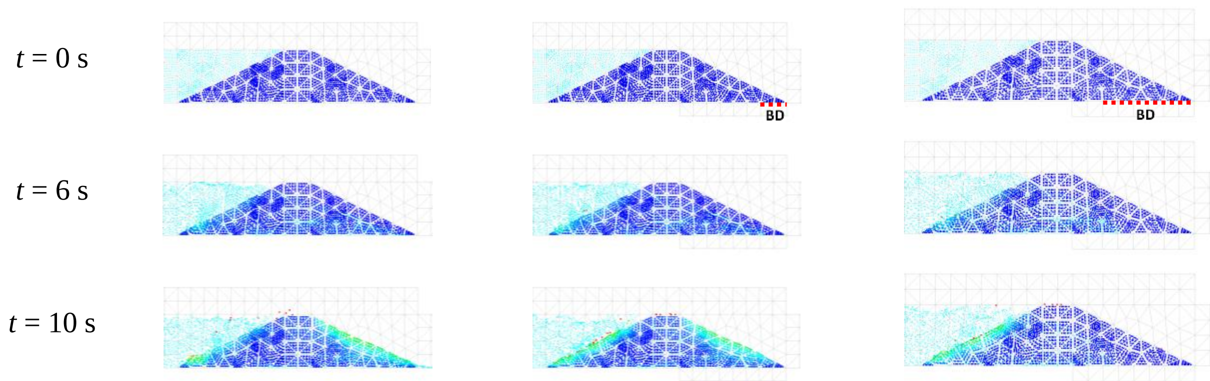

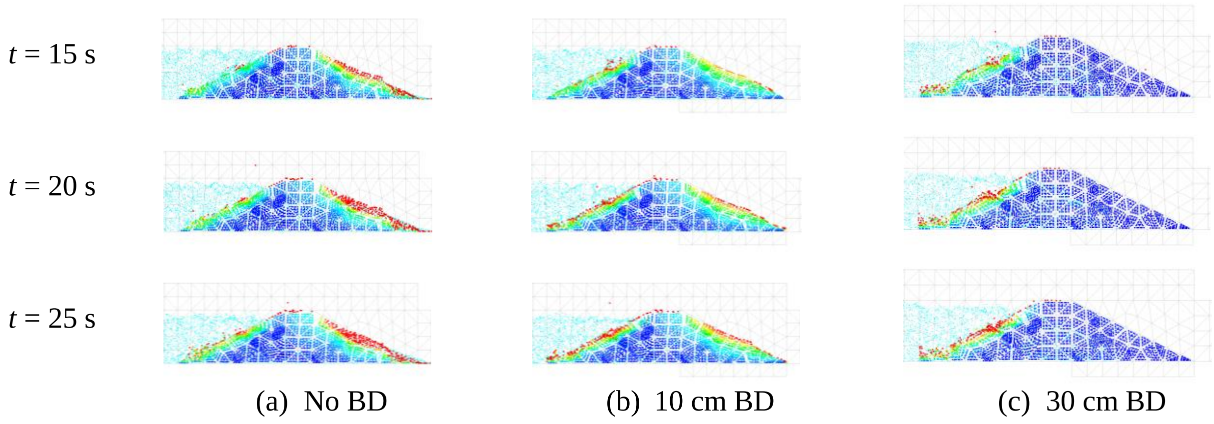

Fig. 9. Solid displacement (in metres) with different BD lengths (0.0 0.02 0.04 0.05)

As mentioned before, the BD was implemented in the simulations as an outflow boundary. We can sum the mass of all the liquid MPs going through the BD outflow boundary, which gives the amount of water collected by the BD. Fig. 10 (a) illustrates the time variations of the drained water mass for cases with various BD lengths. The effect of the BD kicks in earlier with a longer BD, since the seepage line reaches the BD at an earlier stage. The maximum drainage capacity q_{max} also increases with an increase in the BD length, as the curve becomes steeper as the BD length increases.

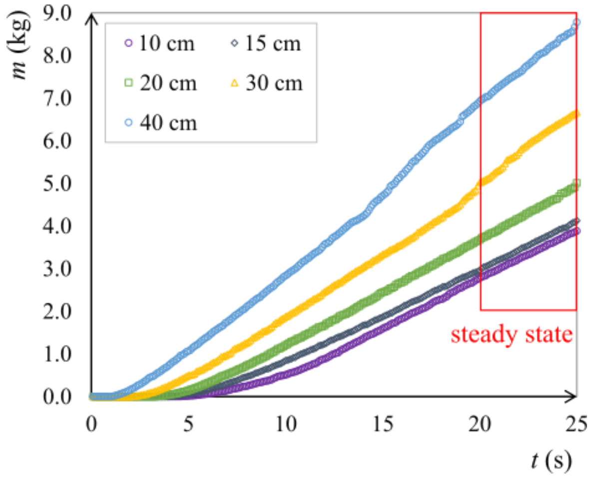

(a) Time variation of the mass of the total drained water with various BD lengths

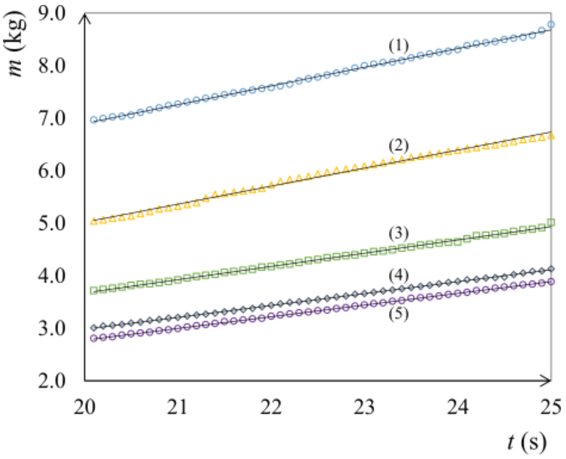

(b) Close-up at the steady state

Fig. 10. Drained water masses versus time with various BD lengths

The slope of the curve in Fig. 10 represents the discharge rate of the drainage system. Anura3D is a 3D programme, so a small width of 0.05 m is specified for the current plane-strain case studies. The calculated drainage capacities Q_{max}, in litre per second, and q_{max} , in meter sequared per second, are listed in Table 2.

Table 2 Maximum drainage capacity for BDs for different lengths

BD length [cm]	Q_{max} [l/s]	q_{max} [m^2 /s]
10	0.22	0.0044
15	0.23	0.0045
20	0.25	0.0050
30	0.34	0.0069
40	0.36	0.0071

Since the dike failure was observed only for simulations with a BD length of 15cm or shorter, the critical unit-width drainage capacities $q_{max,crit}$ for ensuring the dike stability can be considered to be between 0.0045 m^2/s and 0.0050 m^2/s. These values are almost one order of magnitude smaller than the incoming flow rate of 0.04 m^2/s adopted in Schmocker (2011)'s original experiment, confirming that the experiment is indeed about the rapid overtopping failure mechanism.

Evaluation of the surface & core protection

The simulations in this section are intended to qualitatively demonstrate the effects of core protection, shown in Fig. 11 (b), and upstream slope surface protection, shown in Fig. 11 (c). The material properties of the dike were the same as those listed in Table 1 and the protection material differed only at the grain diameter D_p, which was 0.02 mm, i.e. 1% of the dike's grainsize. Therefore, the intrinsic permeability of the protection was only 0.01% of the dike according to Equation 4, i.e. nearly impermeable.

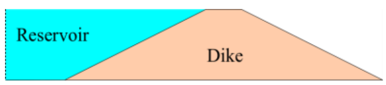

(a) No protection

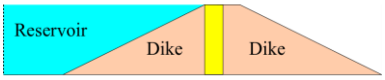

(b) Core protection

(c) Upstream surface protection

Fig. 11. Sketch of protection methods

In these simulations, the reservoir was initially full and the dike was initially dry. A comparison of the advancement of water table inside the dike is given in Fig. 12, where the liquid concentration is plotted to range from from 0 (blue colour) to 0.43 (red colour). Once the seepage flow reached the downstream dike face, slope failure occurred, as seen in Fig. 12(a) corresponding to the situation where there was no protection. With the application of core/surface protection, whose permeability was very low, the seepage path was obstructed and thus dike failure did not occur anymore.

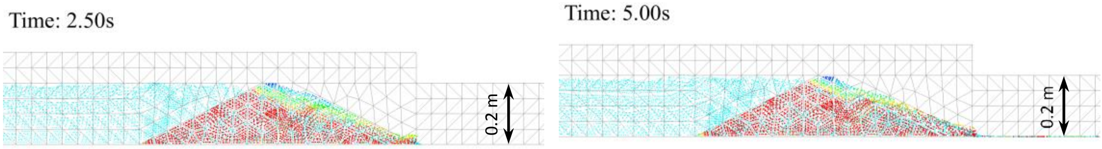

(a) No protection

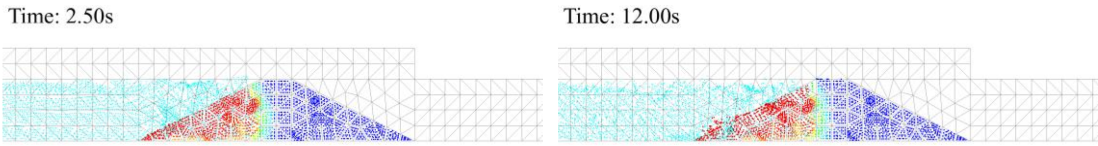

(b) Core protection

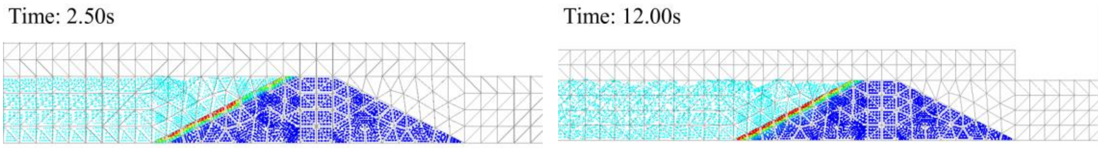

(c) Surface protection

Fig. 12. Comparison of water table advancement inside dike with/without protection (liquid concentration 

)

5. CONCLUSIONS

In this paper, the two-point two-phase version of the Anura3D MPM model was used to study the stability and the ensuing large deformations of non-cohesive dikes due to overtopping and seepage flows. By representing the solid and water constituents with two separate sets of MPs, the model enabled the simulation of relative movement between the water and solid phases and dynamic soil-water interactions.

Simulation results were verified against experimental measurements. The simulation captured the large deformation of the dike profile accurately. Parametric studies were conducted to analyse the dike response under various protections. The effect of the BD location, the maximum capacity of the BD, the effect of core protection and upstream surface protection were all studied in the parametric studies. The following conclusions can be drawn about the dike stability subject to seepage flows and overtopping flows:

- The downstream BD protection outperforms the upstream BD protection.
- The maximum BD capacity plays a key role in the stability of dikes. With an increase in drainage capacity, seepage flow lines no longer reach the downstream dike face, preventing seepage-induced failure.
- The application of a protection layer in the core or on the upstream dike slope effectively obstructed the seepage path and thus avoided the dike failure due to seepage flows.

Through these case studies, the two-point MPM is shown to be a powerful tool for studying problems involving strong coupling between soil and water.

6. ACKNOWLEDGEMENTS

We are grateful to the financial support by the Royal Academy of Engineering UK-China Urban Flooding Research Impact Programme (UUFRIP\100051) and the Royal Society-Newton Mobility Grant (EC\NSFC\191369).

REFERENCES

Abe, K., Soga, K. and Bandara, S. (2013) ‘Material Point Method for Coupled Hydromechanical Problems’, *Journal of Geotechnical and Geoenvironmental Engineering*, 140(3), pp. 1–16.

Alonso, E. E. and Zabala, F. (2011) ‘Progressive failure of Aznalcóllar dam using the material point method’, *Géotechnique*, 61(9), pp. 795–808. doi: 10.1680/geot.9.P.134.

Bandara, S. and Soga, K. (2015) ‘Coupling of soil deformation and pore fluid flow using Material Point Method’, *Computers and Geotechnics*. Elsevier Ltd, 63(1), pp. 199–214.

Chinnarasri, C. *et al.* (2003) ‘Flow patterns and damage of dike overtopping’, *International Journal of Sediment Research*, 18(4), pp. 301–309.

Daniel, D. E. (2007) *The ERP Report: What went wrong and why?* Edited by D. E. Daniel. Civil Engineering.

Ergun, S. (1952) ‘Fluid flow through packed columns’, *Chemical Engineering Progress*, 48, pp. 89–94.

Hager, W. H. (2016) ‘Fluvial dike overtopping : Experimental advances’, in *River Flow 2016*, pp. 12–23.

Huber, L. E., Evers, F. M. and Hager, W. H. (2017) 'Solitary wave overtopping at granular dams', *Journal of Hydraulic Research,* 55(6), pp. 799–812. doi: 10.1080/00221686.2017.1356757.

ICOLD (International Commission on Large Dams). (2013). 'ICOLD bulletin on internal erosion of existing dams, levees and dikes, and their foundations', Internal erosion processes and engineering assessment, Vol. 1, Paris.

Jassim, I., Stolle, D. and Vermeer, P. (2013) 'Two-phase dynamic analysis by material point method', *International Journal for Numerical and Analytical Methods in Geomechanics*, 37(15), pp. 2502–2522. doi: 10.1002/nag.

Martinelli, M. (2016) *Soil-water interaction with material point method*. Delft, the Netherlands.

Martinelli, M. and Rohe, A. (2015) 'Modelling fluidisation and sedimentation using material point method', in *1st Pan-American Congress on Computational Mechanics*. doi: 10.13140/RG.2.1.4638.3445.

Panizzo, A. *et al.* (2005) 'Great landslide events in Italian artificial reservoirs', *Natural Hazards and Earth System Sciences,* 5, pp. 733–740.

Schmocker, L. (2011) *Hydraulics of dike breaching*. ETH ZÜRICH, Switzerland. doi: 10.3929/ethz-a-010782581.

Schmocker, L., Frank, P.-J. and Hager, W. H. (2014) 'Overtopping dike-breach: effect of grain size distribution', *Journal of Hydraulic Research,* 52(4), pp. 559–564. doi: 10.1080/00221686.2013.878403.

Schmocker, L. and Hager, W. (2009) 'Modelling dike breaching due to overtopping', *Journal of Hydraulic Research*, 47(October), pp. 585–597. doi: 10.3826/jhr.2009.3586.

Schmocker, L. and Hager, W. H. (2012) 'Plane dike-breach due to overtopping: effects of sediment, dike height and discharge', *Journal of Hydraulic Research*. Taylor & Francis, 50(6), pp. 576–586. doi: 10.1080/00221686.2012.713034.

Singh, V. P. (1996) *Dam Breach Modeling Technology*. Springer.

Wei, H. *et al.* (2016) 'Overtopping breaching of river levees constructed with cohesive sediments', *Natural Hazards and Earth System Sciences*, 16(7), pp. 1541–1551. doi: 10.5194/nhess-16-1541-2016.

Więckowski, Z. (2013) *Enhancement of the Material Point Method for Fluid-Structure Interaction and Erosion, Deltares*. Delft, the Netherlands.

Yerro, A., Alonso, E. E. and Pinyol, N. M. (2015) 'The material point method for unsaturated soils', *Géotechnique*, 65(3), pp. 201–217. doi: 10.1680/geot.14.P.163.

Zhao. (2019). 'Improvements of MPM and its applications in modelling rapid soil/water movements', PhD thesis, University of Cambridge, 185 pages.

Zhao, X. *et al.* (2019) 'Development of in/outflow boundary conditions for MPM simulation of uniform and non-uniform open channel flows', *Computers & Fluids*. Elsevier Ltd, 179, pp. 27–33. doi: 10.1016/j.compfluid.2018.10.007.

Zhao, X. and Liang, D. (2016) ‘MPM modelling of seepage flow through embankments’, in *Proceedings of the Twenty-Sixth (2016) International Ocean and Polar Engineering Conference*. Rodos, Greece, pp. 1161–1165. doi: 10.13140/RG.2.2.33519.23208.

Zhu, Y. (2006) *Breach Growth in Clay-Dikes*. Delft University of Technology.